Chemical Geology 497 (2018) 100–114

Contents lists available at ScienceDirect

Chemical Geology

journal homepage: www.elsevier.com/locate/chemgeo

Evolution of planar fractures in limestone: The role of flow rate, mineral heterogeneity and local transport processes

Catherine Noiriel[a,*], Hang Deng[b]

[a] Géosciences Environnement Toulouse, Observatoire Midi-Pyrénées, Université Paul Sabatier, CNRS, IRD, Université de Toulouse, 14 avenue Edouard Belin, F-31400 Toulouse, France

[b] Energy Geosciences Division, Earth and Environmental Sciences Area, Lawrence Berkeley National Laboratory, Berkeley, CA 94720, United States

ARTICLE INFO

Editor: Karen J.

Keywords:
Reactive transport
Dissolution
Mineral heterogeneity
Fracture
Kinetics
Modeling
X-ray micro-tomography

ABSTRACT

The processes that affect the evolution of fracture geometry and reactive transport in limestone fractures were evaluated using an integrated experimental and modeling approach. Flow-through experiments were performed to investigate the alteration of three artificially made planar limestone fractures, which were exposed to HCl-acidified water flow (pH 3.8 ± 0.1) at three different rates. Reactive infiltration instability developed in the fractures because of small fracture aperture variations and naturally occurring heterogeneity in the rock, i.e., the presence of clay spots of higher porosity. The dissolution regime changed from conical to dominant and ramified wormhole with increasing flow rate, i.e., Péclet number. Maps of fracture aperture obtained from X-ray micro-tomography imaging, together with measurements of permeability and analyses of fluid chemistry, provided experimental constraints for modeling. Numerical simulations were performed using a 2.5D continuum reactive transport model to examine the development of flow patterns and the reactivity and permeability evolution over time, and to interrogate the impacts of fluid reactivity, mineral heterogeneity and diffusive boundary layer. The modeling results showed that fracture alteration is very sensitive to initial fluid reactivity and mineralogical heterogeneity, in addition to flow rate. The changes of local transport processes during fracture opening also affected the reactivity of the fractured samples.

1. Introduction

Understanding fracture alteration by geochemical fluids and the subsequent evolution of flow and reaction is a critical research area relevant to CO_2 sequestration, unconventional hydrocarbon production, reservoir stimulation, geothermal energy and nuclear waste storage (Aydin, 2000; DePaolo and Orr, 2008; Griffiths et al., 2016; Pyrak-Nolte et al., 2015). Such anthropogenic activities may introduce strong geochemical disequilibrium and high injection rates compared to natural geochemical and flow conditions. Previous studies have shown that flow rate and fluid reactivity both play an important role in controlling channel development in dissolving rocks, and thus the resulting changes in hydraulic properties of the rocks (Daccord et al., 1993; Golfier et al., 2002; Hoefner and Fogler, 1998; Luquot and Gouze, 2009). For instance, in acid fracturing, excessive acid leak-off and consumption through wormholes are considered to be the main reason that limits fracture propagation and live acid penetration distance (Bazin, 2001; Hung and Sepehrnoori, 1989; Zhang et al., 2014).

Different dissolution regimes have been identified and correlated with dimensionless numbers, e.g., Péclet (*Pe*) and Damköhler (*Da*) numbers (e.g., Daccord et al., 1993; Golfier et al., 2002; Hoefner and Fogler, 1998; Ortoleva et al., 1987a; Steefel and Lasaga, 1990; Szymczak and Ladd, 2009). In fractures, the transverse Péclet number compares the advective transport rate along the fracture to the diffusive transport rate across fracture walls, and can be defined as (e.g., Mourzenko et al., 1996):

$$\mathrm{Pe} = \bar{v}a/D_m, \quad (1)$$

where $\bar{v}$ is the average fluid velocity ($m{\cdot}s^{-1}$), D_m is the molecular diffusion ($m^2{\cdot}s^{-1}$) and a is the fracture aperture (m). For example, experiments in artificial analog fractures (Detwiler et al., 2003) have underlined the strong dependence of dissolution patterns on the Péclet number, with ramified wormhole and uniform dissolution observed at *Pe* values of 54 and 216, respectively. The observations were also confirmed by the modeling study of the experiments (Szymczak and Ladd, 2004).

Da compares the ratio between the chemical reaction rate and the diffusive mass transfer rate, and can be defined for heterogeneous phase

* Corresponding author.
E-mail addresses: catherine.noiriel@univ-tlse3.fr (C. Noiriel), hang.deng@lbl.gov (H. Deng).

https://doi.org/10.1016/j.chemgeo.2018.08.026
Received 23 April 2018; Received in revised form 20 August 2018; Accepted 28 August 2018
Available online 01 September 2018
0009-2541/

reactions as (e.g., Dijk and Berkowitz, 1998):

$$\mathrm{Da} = k_r L^{*2}/D_m, \quad (2)$$

where k_r is a first-order kinetic rate constant (s^{-1}), and L^* is a characteristic length (m). Other expressions are available for zero- or second-order reactions. Overall, fracture channelization is observed at intermediate *Da* values when reaction rate and transport rate are comparable. In contrast, uniform fracture dissolution is observed when the transport rate is much higher and the system is surface reaction controlled (low *Da*), and localized dissolution is observed when the reaction rate is faster and the system is transport-limited (high *Da*).

Although the concepts of Péclet and Damköhler numbers provide a unified framework to analyze the evolution of fractures in different transport regimes, these analyses are typically limited to simplified geochemical systems, geometries, and flow conditions. Traditional definitions of *Pe* and *Da* (e.g., Eqs. (1) and (2)) also do not account for the observations that *Pe* and *Da* may vary spatially and temporally (Noiriel, 2015). In addition, as revealed by several experimental and numerical studies, other processes not included in *Pe* and *Da* can also affect the evolution of fractures, including the initial structural heterogeneity, mineral impurities (even in nominally pure rocks), and heterogeneity in mineral composition.

Initial geometry has also been reported as one of the factors that largely control the phenomenon of self-organization (Ortoleva et al., 1987b). Regions of higher permeability attract more fluid, which leads to more dissolution in these areas. Consequently, permeability increases locally, and the process is amplified over time through a positive feedback between flow and chemical reactions. Eventually, preferential channels develop in the fractures. Minor structural heterogeneity initially present in fractures, e.g., vugs, can influence the localization of dissolution patterns (Elkhoury et al., 2013), but it is difficult to decipher whether they can influence the dissolution regime. Cheung and Rajaram (2002) have observed different dissolution regimes, from conical to ramified wormholes by increasing the fracture aperture roughness, σ_a/a_m, (with σ_a the root mean square of the mechanical aperture, and a_m the mechanical aperture) in their simulations. However, some numerical studies have shown that reactive infiltration instability can develop in planar fractures of uniform aperture in homogeneous material (Osselin et al., 2016; Starchenko et al., 2016; Szymczak and Ladd, 2012). Some investigators have also reported that the statistical properties of the evolving dissolution patterns were insensitive to fracture surface roughness or correlation length of the initial aperture field (Upadhyay et al., 2015). A lack of experimental data that investigate the role of geometry on the dissolution patterns is nevertheless worth mentioning.

Rock composition and texture also have a large impact on dissolution patterns (Andreani et al., 2009; Deng et al., 2016; Garcia-Rios et al., 2017; Gouze et al., 2003; Noiriel et al., 2013; Noiriel et al., 2007a; Noiriel et al., 2007b). The flow regime corresponding to a given dissolution pattern can be different in a mineralogically heterogeneous sample from what would be expected if no mineral heterogeneity is present (Chen et al., 2014; Deng et al., 2018). Large differences in mineral dissolution rates can result in the development of micro-porous altered layers or surface asperities. In both cases, the dissolution patterns and the hydraulic evolution of the fractures can be affected. While the altered layer tends to slow down mass transfer at the mineral fronts (and thus affecting both *Da* and *Pe* if considering effective diffusion instead of molecular diffusion in Eqs. (1) and (2)), the presence of non-dissolving asperities can influence channel development and fracture hydraulic properties in different ways depending on the confining pressure (e.g., Elkhoury et al., 2013). Additionally, the mechanical strength of the micro-porous altered layer may have an impact on flow localization. For example, channelization that was not correlated to the initial flow field was observed in a slightly argillaceous limestone fracture (90% calcite) and was attributed to removal of the micro-porous altered matrix (Noiriel et al., 2007a).

Overall, the concepts of *Pe* and *Da* are useful, but applying them in investigations of fracture dissolution regimes and subsequent evolution of hydraulic properties can be challenging because their values are affected by multiple variables and processes. To better evaluate the extent to which *Pe* and *Da* can be used as a guide for fracture evolution studies, it is important to isolate each factor to avoid cross effects between the processes, and to investigate the impacts of factors that are not included in traditional *Pe* and *Da* definitions.

The objectives of the present study are to investigate how the flow rate and thus *Pe* affect fracture dissolution regimes, and also to identify and to examine the factors that affect fracture evolution but are not explicitly accounted for in traditional *Pe* and *Da* definitions. For this purpose, we investigated the evolution of geometry, flow, and reactions during flow-through dissolution experiments in planar limestone fractures of the same initial average aperture (a_0) at three different initial Péclet numbers (Pe_0). Planar fractures were used instead of artificially-induced rough fractures to ensure that the geometry is comparable between experiments. In addition to measurements of fracture permeability and fluid chemistry, X-ray micro-tomography was used to characterize the morphology of the channels developed in the fractures. Experimental results were then used to constrain reactive transport modeling. Different simulation configurations were tested to evaluate the impacts of three factors - fluid reactivity, mineral heterogeneity, and local transport processes - on self-organization and channel development in fractures.

2. Material and methods

2.1. Reactive flow experiments in fractures

The flow-through experiments were performed in saw-cut single fractures in a low porosity and matrix permeability micritic limestone. The rock has a very low clay content (no clay was detected with X-ray diffraction), but sporadic clay spots and clay layers of higher porosity are visible on the fracture surfaces and evident in the X-ray micro-tomography images. Three core samples of 9 mm in diameter and 15 mm long, named FRAC1 to FRAC3, were prepared from two halves of a sawn block that were polished using 800-grit SiC paper, put back together, and cored to produce planar fractures. The initial aperture, a_0, was set to ~20 μm by inserting calibrated epoxy-glued wedges on the cylinder edges. This treatment also prevented any mechanical closure of the fractures. The resulting fracture width is about 6 mm (Table 1). The top and bottom part of the cores apart from the fracture inlet and outlet were also coated with epoxy resin so that they remain unreacted during the experiments.

The influent fluid was an acidic solution of pH = 3.8 ± 0.1 with

Table 1
Summary of the experimental conditions for the three fractured samples FRAC1 to FRAC3.

Sample	Experiment duration (h)	Flow rate Q ($cm^3 \cdot h^{-1}$)	Length L (mm)	Width l (mm)	a_0 (μm)	Pe_0	$\bar{v}_0$ ($m \cdot s^{-1}$)
FRAC1	164 h 30 min	1.2	15.1	6.4	20[a]	7	$2.6\ 10^{-3}$
FRAC2	55 h	102	15.2	6.0	20[a]	598	$2.4\ 10^{-1}$
FRAC3	26 h 30 min	300	14.9	6.4	20[a]	1648	$6.5\ 10^{-1}$

[a] An initial mechanical aperture of 20 μm is assumed for the different fractures.

0.01 M NaCl, prepared using a 32 wt% hydrochloric solution, reagent-grade salt and deionized water. After vacuum saturation with deionized water, the samples were injected with the influent using a piston pump at a constant flow rate, Q, of 1.2 (FRAC1), 102 (FRAC2) and 300 (FRAC3) $cm^3 \cdot h^{-1}$ for 164 h 30, 55 h, and 26 h 30, respectively. The initial conditions of the experiments are summarized in Table 1.

The effluent pH was continuously recorded, and water samples were regularly collected for chemical analyses by inductively coupled plasma atomic emission spectrometry (ICP-AES). The hydraulic aperture, a_h, was calculated from the continuous measurements of differential pressure between the sample inlet and outlet, ΔP ($kg \cdot m^{-1} \cdot s^{-2}$), using the cubic law (e.g., Zimmerman and Yeo, 2000):

$$a_h = \sqrt[3]{12Q\mu L/l\Delta P} \tag{3}$$

where l is the fracture width (m), L is the fracture length (m), and μ is water viscosity ($kg \cdot m^{-1} \cdot s^{-1}$). Experiments FRAC2 and FRAC3 were terminated when ΔP approached zero and could not be reliably measured.

Changes in fracture aperture were measured from the X-ray microtomography (XMT) data sets that were collected after the experiments at the European Synchrotron Radiation Facility, BM05 beamline (Grenoble, France). The pixel size is 5.25 μm for FRAC1 and FRAC2 and 4.91 μm for FRAC3. As the vertical field of view of the beam was smaller than the sample length, three or four vertical scans were taken for each sample, including the sample inlet and outlet, and the area next to the inlet. Nevertheless, a small portion of each fracture is missing (see further in Fig. 3).

No fracture aperture map before the reactive flow experiments is available, but aperture measurements in the initially glued and thus unreacted fracture edges confirmed that the aperture was initially about 20 μm. The 2D maps of the fracture aperture, defined as the distance normal to the fracture walls, were derived from the 3D data after image segmentation (see Noiriel et al., 2013 for more details about image processing). The mechanical aperture, a_m, is defined as the mean of the local geometric apertures (e.g., Renshaw, 1995):

$$a_m = \langle a \rangle_{yz} = \frac{1}{Ll} \int_{y=0}^{l} \int_{z=0}^{L} a(y,z)\,dydz \tag{4}$$

The average rate of fracture opening, $\bar{r}_{XMT}$ ($\mu m \cdot s^{-1}$), can be derived from the XMT data:

$$\bar{r}_{XMT} = (a_m - a_0)/\Delta t, \tag{5}$$

where Δt is the duration of the experiment. Similarly, the average growth rate of a channel, $\bar{r}_w$, was calculated by restricting the measurements of aperture to the channelized region. The maximum growth rate within a channel, $\bar{r}_{w-\max}$, was calculated using local maximum aperture in the channelized region.

The extent of reaction, as quantified by the volume of calcite removed from the rock matrix during the reactive flow experiments ($\delta V_{calcite}$, m^3), can also be evaluated using fluid chemistry:

$$\delta V_{calcite} = -v_{calcite} \times F_{Ca} \times \delta t = -v_{calcite} \times Q \times \delta(\Delta \mathrm{Ca}), \tag{6}$$

where F_{Ca} is the flux of calcium at the sample outlet ($mol \cdot s^{-1}$), $v_{calcite}$ is the molar volume of calcite ($m^3 \cdot mol^{-1}$), and ΔCa measures the difference between the effluent and influent calcium concentrations, i.e. $[\mathrm{Ca}]_{out} - [\mathrm{Ca}]_{in}$ ($mol \cdot m^{-3}$). The dissolution rate derived from chemical analyses, r_c, can also be expressed in term of fracture opening rate, i.e. $\delta a_c/\delta t$ ($\mu m \cdot s^{-1}$), where a_c is the so-called chemical aperture (Noiriel et al., 2007a) defined at time t_i as:

$$\begin{aligned} a_c(t_i) &= a_0 + \int_{t=0}^{t=t_i} \frac{\delta a_c}{\delta t} dt = a_0 + \frac{1}{A_s} \int_{t=0}^{t=t_i} \frac{\delta V_{calcite}}{\delta t} dt \\ &= a_0 + \frac{Q \times v_{calcite}}{A_s} \int_{t=0}^{t=t_i} \delta(\Delta \mathrm{Ca})\,dt, \end{aligned} \tag{7}$$

where a_0 is the initial fracture aperture, A_s is the surface area of the fracture wall. The average rate of fracture opening, $\bar{r}_c$ ($\mu m \cdot s^{-1}$), is defined as:

$$\bar{r}_c = (a_c - a_0)/\Delta t \tag{8}$$

The calculation of a_c gives additional information about the reactivity of the samples based on mass balance, and can be used to evaluate the accuracy of the XMT imaging, as a_m and a_c should be similar.

2.2. Flow and reactive transport modeling

2.2.1. Model description

The 2.5D reactive transport model (Deng et al., 2016; Deng et al., 2017) used to simulate fracture evolution as a result of mineral reaction is implemented in CrunchFlow, a multi-component reactive transport code (Steefel et al., 2015). Here, we only provide a brief summary of the key features of the model that are relevant to this study.

In the model, the fracture is discretized into a 2D mesh within the fracture plane, which means that the initial aperture maps derived from XMT images, if available, can be used directly. Each grid cell is a continuum, where the local porosity ($\phi_{y,z}$) and permeability ($k_{y,z}$) are determined by the local fracture aperture ($a_{y,z}$), i.e.:

$$\phi_{y,z} = \frac{a_{y,z}}{d_x}, \tag{9}$$

and

$$k_{y,z} = \frac{a_{y,z}^3}{12 d_x}, \tag{10}$$

where d_x (m) is the thickness of the simulated domain in the dimension perpendicular to the fracture plane. Since all physical properties are normalized against d_x, its value does not affect the simulations.

The fluid velocity in the fracture, $\mathbf{v}$ (the components of which are v_y and v_z) ($m \cdot s^{-1}$), is solved using Darcy's law:

$$\phi \mathbf{v} = \frac{k \nabla P}{\mu}, \tag{11}$$

where ∇P is the pressure gradient ($kg \cdot m^{-2} \cdot s^{-2}$), and μ is the dynamic viscosity with a value of $1.0\ 10^{-3}$ Pa·s. Given that the permeability used in the calculation is related to local aperture by the cubic law (Eq. (3)), it is equivalent to solving the depth-averaged Reynolds equation that is commonly used for the quantification of flow field in discrete fractures (e.g., Detwiler et al., 2003). It is assumed that there is no variation in fluid density or viscosity, which is justified by the relatively small change in fluid composition during the experiments. Darcy's equation is discretized using the integrated finite difference method.

The governing advection-diffusion-reaction equation is given by:

$$\frac{\partial(\phi \Psi_i)}{\partial t} = \nabla \cdot (\phi \mathbf{D} \nabla \Psi_i - \mathbf{v} \Psi_i) - \sum_m \nu_{i,m} R_m \Big/ \left(d_x d_y d_z \right), \tag{12}$$

where Ψ_i is the total concentration of component i, $\mathbf{D}$ is the dispersion tensor ($m^2 \cdot s^{-1}$), and R_m is the dissolution reaction rate for mineral m ($mol \cdot s^{-1}$), and $\nu_{i,m}$ is the stoichiometric coefficient for the reaction. The equation uses the same discretization as Darcy's equation. The three terms on the right hand side capture the changes in concentration caused by transport, flow, and reactions, respectively. In this study, the dispersion tensor considers only molecular diffusion, neglecting hydrodynamic dispersion, given that the discretization is fine enough to capture velocity variations in the fracture plane.

The reaction rate of minerals is described by Lasaga (1981):

$$R_m = A_m k_m (1 - \Omega), \tag{13}$$

where A_m and k_m are the reactive surface area (m^2) and the rate constant of the mineral ($mol \cdot m^{-2} \cdot s^{-1}$), respectively, and Ω is the saturation

index (Ω = IAP/K_{sp}, where K_{sp} is the solubility and IAP is the ion activity product). For calcite, the rate constant is a function of pH and carbonic acid concentration (Chou et al., 1989; Morse and Arvidson, 2002; Plummer et al., 1978) and can be written as:

$$k_{cal} = k_1 a_{H+} + k_2 a_{CO2} + k_3 \quad (14)$$

where k_1, k_2, and k_3 are kinetic coefficients.

The reactive surface area is determined in this study by the geometric surface area of the fracture surface in the continuum grid cell, and is corrected by a surface roughness factor (SRF) to account for subgrid surface roughness:

$$A_m = A_{geo}\mathrm{SRF} = 2d_y d_z \mathrm{SFR} \quad (15)$$

where A_{geo} is the geometric surface area of the fracture walls, and d_y and d_z are the size of the grid cell.

The 2.5D model does not solve for velocity and concentration profiles across the fracture aperture explicitly. However, it allows consideration of such gradients across the fracture aperture by integrating analytical solutions as detailed in Deng et al. (2017) and briefly introduced in the following section.

2.2.2. Simulation setup

In this study, the model is applied to examine the underlying processes that have resulted in the experimentally observed alteration of the fractures at the three flow rates. Even though an exact match to the experimental observations is impossible due to the lack of precise knowledge of the initial fracture geometries, the simulations allow numerical experiments to isolate each controlling factor. Three sets of simulations were set up to investigate the potential impacts of (i) the reaction rates, (ii) mineral heterogeneity, and (iii) transport limitation between the fracture walls. All the simulations are summarized in Table 2.

Initial fracture geometries are 2D random fields of the same size and average aperture as FRAC1 to FRAC3 (Table 1). The random fields were generated using the same method as Deng et al. (2018), and will be referred to as FRAC1_sim to FRAC3_sim (Fig. 1). The aperture fields follow a lognormal distribution with an average aperture of 20 μm and a standard deviation of 5 μm, considering that the experimental fracture walls were globally flat and smoothened. The small variation in the fracture aperture reflects the grain size effect and roughness that may be introduced during sample preparation. Given the small aperture variation, no spatial correlation was considered. A grid cell size of 0.1 mm by 0.1 mm was used in all simulations.

The rock matrix composition was simplified in the simulations, with calcite as the only reactive mineral phase. The influent fluid used in all simulations has the same chemistry composition as in the experiments. Given that the inlet fluid has a low concentration in carbonic acid and the outlet fluid remains far from equilibrium, the calcite reaction rate is dominated by the pH effect, and thus only the first term of Eq. (14) was considered. The flow boundary conditions used for each aperture field follow the corresponding experiment, with a constant volumetric flow rate at the inlet (Table 1), and uniform pressure (P = 0.1 MPa) at the outlet.

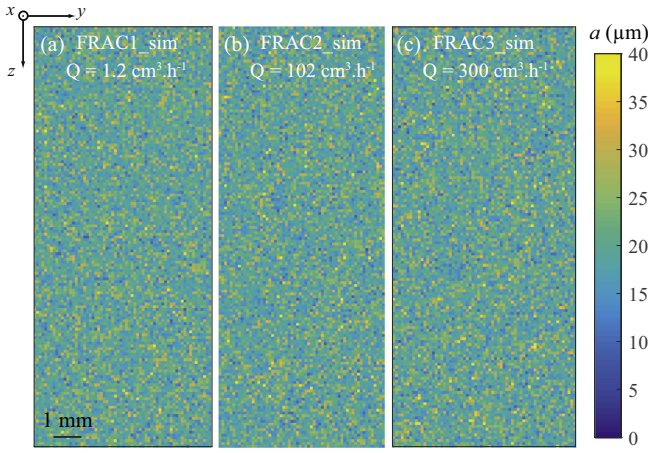

Fig. 1. (a)–(c) Initial randomly generated fracture geometries FRAC1–3_sim used in the simulations and corresponding to the experiments FRAC1–3.

The first set of simulations focuses on the impacts of calcite dissolution rate, and thus mineral spatial heterogeneity and diffusion limitation across the fracture aperture were not considered. Uncertainties in calcite dissolution rate were explored by varying the kinetic coefficient k_1 in Eq. (14) and the surface roughness factor and thus reactive surface area (Eq. (15)). Comparison between the simulation results and the experimental observations allow a better constraint on the input parameters in the following simulations.

In the second set of simulations, initial mineral heterogeneity is considered by varying the spatial distribution of calcite volume fraction. A small fraction of the grid cells were assigned a lower calcite volume fraction (60%) to represent the clay spots (Fig. 2). This treatment means that the clay fraction was assigned as void space, which is equivalent of assuming that the clay minerals would be removed immediately after the dissolution of calcite and initially unreactive. This assumption is justified by the lack of an altered layer at the fracture surface in the high flow rate experiments. This treatment is also equivalent to using a large erosion rate in the erosion model developed in Deng et al. (2017) that captures clay mineral removal from the rock matrix due to particle mobilization and transport.

Two types of spatial distribution were considered. One type of the spatial distribution uses small clusters of grid cells to represent the clay spots observed in the XMT data sets. Random fields with spatial correlation of 1500 μm were generated and segmented to create the masks for the clay spots. The threshold value was chosen such that the total

Table 2
Summary of the modeling cases. For each modeling case, three fractures corresponding to FRAC1–3 were simulated (FRAC1_sim to FRAC3_sim).

	Reference of the simulations (appended to FRAC1–3_sim)	Kinetic rate	Surface roughness factor	Mineral heterogeneity	Diffusion limitation across aperture
1st set	_k_1-Chou	Chou*	SRF = 1	–	–
	_k_1-Plummer	Plummer**	SRF = 1	–	–
	_k_1-Deng	Deng***	SRF = 1	–	–
	_SRF4	Chou*	SRF = 4	–	–
	_SRF10	Chou*	SRF = 10	–	–
2nd set	_MH-c1	Chou*	SRF = 4	Small randomly generated clusters with lower calcite volume	–
	_MH-c2	Chou*	SRF = 4	fraction representing clay spots (3% of the fracture surface)	–
	_MH-c3	Chou*	SRF = 4		–
	_MH-b	Chou*	SRF = 4	Two vertical narrow bands with lower calcite volume fraction representing clay layers (10% of the fracture surface)	–
3rd set	_DBL	Chou*	SRF = 4	–	Considered

The names are given in reference to the work of: *Chou et al. (1989), **Plummer et al. (1978), and ***Deng et al. (2015).

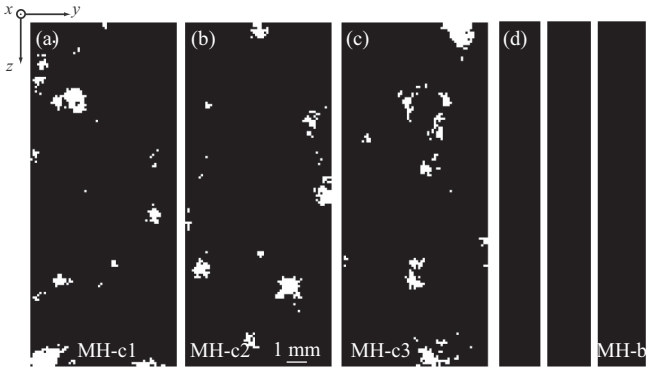

Fig. 2. Masks of the clay spots (in white), with (a)–(c) clustered (MH-c1, MH-c2, and MH-c3) or (d) layered (MH-b) distributions used in the set of simulations accounting for mineral heterogeneity.

area of the clusters accounts for ~3% of the fracture surfaces as estimated from subsections of the XMT data. Three masks, MH-c1 to MH-c3, were generated for the clustered mineral heterogeneity to examine the sensitivity of the dissolution patterns to the spatial distribution of clay spots. The other type of the spatial distribution (MH-b) assumes a highly organized pattern. Two narrow bands (300 μm wide each) with low calcite volume fraction along the flow direction were placed with equal distance to the closest fracture edge and each other to represent the extreme scenario when mineral heterogeneity and flow direction (i.e., the direction of the channel) are highly correlated.

The third set of simulations accounts for the diffusion limitation in the diffusive boundary layer (DBL). This arises from the velocity gradient and the resulting concentration gradient across the fracture aperture, and can be substantial in large apertures. The diffusion limitation due to the boundary layer is accounted for by introducing a diffusion-controlled reaction rate:

$$R_{diff} = \frac{D_0 Sh}{2a}([j] - [j]_s), \tag{16}$$

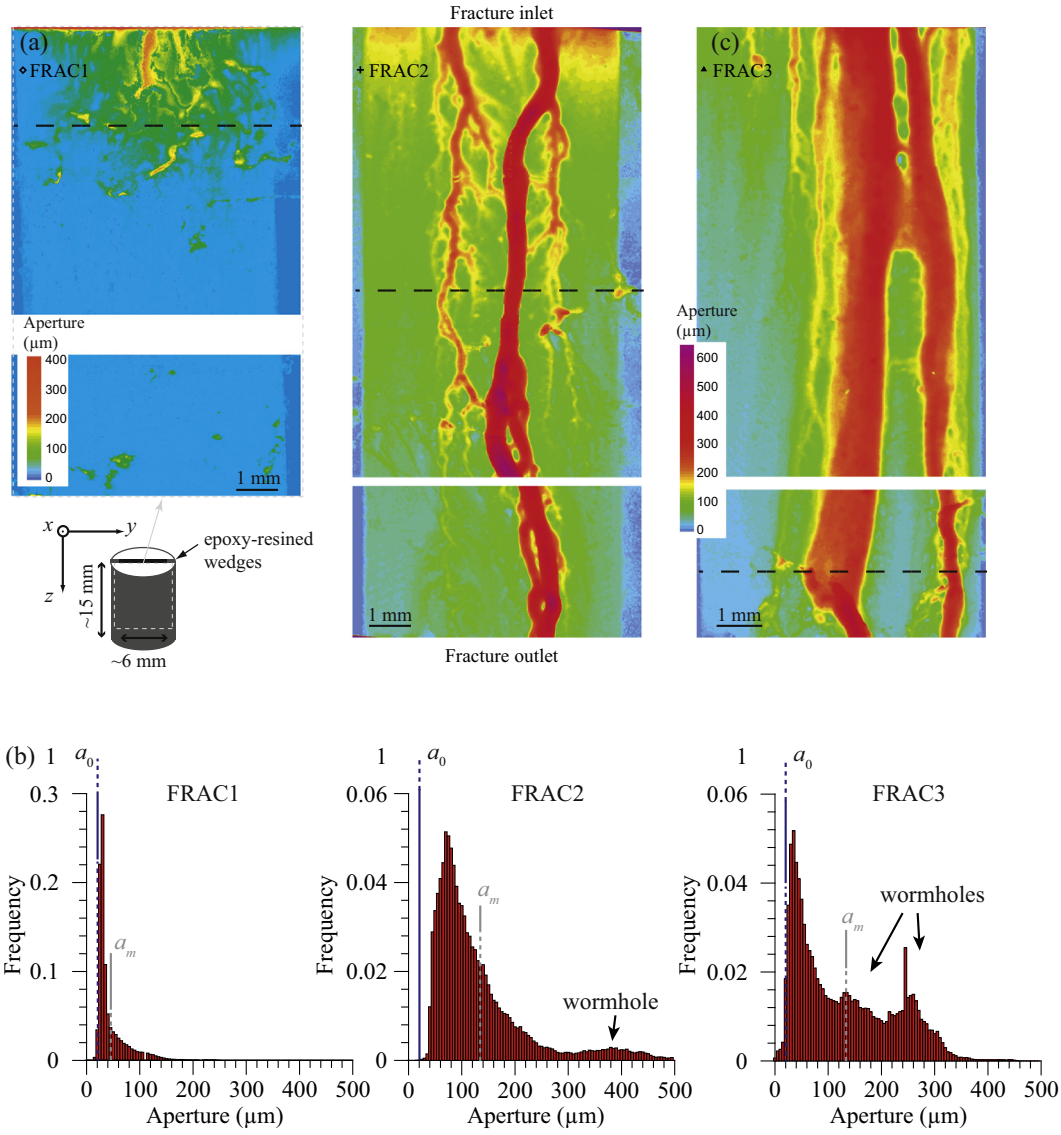

Fig. 3. (a) Aperture maps obtained from XMT after experiment for the three samples FRAC1, FRAC2, and FRAC3; the dotted lines indicate the position of the cross-sections shown further in Fig. 4. (b) Corresponding histograms of aperture; the initial aperture (a_0) and average aperture (a_m) are highlighted in the figure. A small proportion of the fractures (in white) that was not imaged is missing and not included in the calculations.
[Adapted with permission from Noiriel and Daval (2017). Pore-Scale Geochemical Reactivity Associated with CO_2 Storage: New Frontiers at the Fluid-Solid Interface. Accounts of Chemical Research 50, 759–768, Fig. 6; copyright (2017) American Chemical Society.]

where D_0 is the diffusion coefficient, and Sh is the Sherwood number that is typically used to account for the transport gradients between fracture surface and the bulk fluid, $[j]$ is the concentration of species j, and $[j]_s$ is the concentration at the fracture surface. Here, $[j]_s$ was assumed to be the equilibrium concentration. Sherwood number is a function of reaction rate and velocity profile across the aperture, and asymptotic values have been reported (Gupta and Balakotaiah, 2001). A value of $Sh = 8$ was used in the simulations following Szymczak and Ladd (2012). The effective reaction rate, R_{eff} is dominated by the lesser of the surface reaction rate (R_{surf}) and the diffusion-controlled reaction rate (R_{diff}):

$$R_{eff} = \frac{1}{\frac{1}{R_{diff}} + \frac{1}{R_{surf}}} \quad (17)$$

This formulation is similar to what was used for the diffusion limitation of the altered layer, which was first introduced in the 2.5D model (Deng et al., 2016), but the diffusion-controlled reaction rate is determined by the fracture aperture and the molecular diffusion coefficient instead.

In addition, the three post-reaction aperture maps from the experiments were also used as input data for flow simulations, to inform respective flow patterns and fracture hydraulic apertures (a_{h-sim}). The missing data in the aperture maps for FRAC2 and FRAC3 were linear interpolation of the neighboring sections. For FRAC1, as there was no change in the fracture opening along the flow axis across the missing part, the aperture values near the outlet were used to fill the missing data.

3. Results

3.1. Experimental results

3.1.1. Fracture geometry evolution

The 2D aperture maps for the different fractures after the experiments are presented in Fig. 3. The initial aperture field was evaluated from the unreactive edges of the samples, with an average value of 20 μm for all fractures. Some higher apertures were observed at the clay spots or clay layers of higher porosity (Fig. 4).

The dissolution patterns are different between the experiments, but they all reveal the phenomenon of channelization, from conical wormhole (FRAC1), to dominant wormhole (FRAC2) and ramified wormhole (FRAC3). The flowpaths are also dependent on the initial heterogeneity in the fracture apertures. Fluid localization is promoted at the clay spots where the porosity is initially higher (Figs. 3a and 4). Consequently, the fracture surfaces become asymmetric, with channels

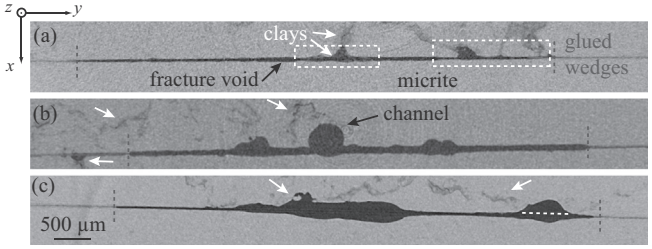

Fig. 4. Cross sections in (a) fracture FRAC1 (sample top), (b) FRAC2 (sample middle) and (c) FRAC3 (sample bottom) at the locations indicated in Fig. 3, showing the influence of the initial mineral heterogeneity, i.e. clay spots (white arrows) of higher porosity, on the dissolution and fluid localization process. Low grey level is the fracture void, high grey level is the limestone matrix (micrite), and the intermediate grey level denotes the clayey areas of higher porosity or fracture wedges (on the edges). For FRAC1, clays remain in the fracture void (dotted white rectangle). Note the dissymmetry in the channel growth process (dotted white line) across the fracture FRAC3 thanks to the presence of clays.

Table 3
Measurements of mechanical aperture a_m using XMT, hydraulic aperture a_h from differential pressure record, and chemical aperture a_c calculated from mass balance, for the three fractured samples before and after the experiment. Comparison with the hydraulic aperture a_{h-sim} calculated from the flow simulations of post-reacted fractures.

Time	Aperture (μm)	FRAC1	FRAC2	FRAC3
Before experiment	a_m	20[a]	20[a]	20[a]
	a_h	14	21	15
After experiment	a_h	11	90	120
	a_m	44	133	134
	a_c	42	136	132
Flow simulations	a_{h-sim}	33	183	171

[a] An initial mechanical aperture of 20 μm is assumed for the different fractures.

preferentially forming in the portions of the fracture walls that contain the clay spots (Fig. 4b,c). In addition, dissolution is more pronounced near the inlet of the samples (Fig. 3), where chemical disequilibrium is higher and the pH of the injected solution is lower.

The aperture distribution changes from quasi-uniform to either long-tailed (FRAC1), bimodal (FRAC2), or trimodal (FRAC3), due to channel development (Fig. 3b). Although the mechanical aperture is very similar for FRAC2 and FRAC3 at the end of the experiment (133 and 134 μm, respectively, see Table 3), the maximum aperture is larger for FRAC2, which has a single dominant channel, compared to FRAC3, where two main coalescing channels are observed.

3.1.2. Effluent chemistry

The extent of the reaction was also examined using the effluent Ca concentration. Fig. 5 shows that $[Ca]_{out}$ remains almost equal to $2.9\ 10^{-4}$ M during the experiment for FRAC1, whereas it decreases from $1.7\ 10^{-4}$ to $2.0\ 10^{-5}$ M for FRAC2, and from $1.4\ 10^{-4}$ to $1.8\ 10^{-5}$ M for FRAC3. The solutions remain largely undersaturated with respect to calcite, with a saturation index (log Ω) ranging at the end of the experiment from −10.5 for FRAC3 to about −1.0 for FRAC1.

While $[Ca]_{out}$ decreases as flow rate increases, the opposite trend is observed for the fluxes of calcium (Fig. 5b,c). F_{Ca} at the beginning of the experiment is up to two orders of magnitude higher for flow rates of 102 and 300 $cm^3 \cdot h^{-1}$ than for FRAC1 (Fig. 5c). At the high flow rates, dissolution rate is promoted by the rapid renewal of fluid within the fracture, which maintains a lower pH at the outlet (3.9 and 3.8 for FRAC2 and FRAC3, respectively) (Fig. 5b). For FRAC2 and FRAC3, however, F_{Ca} drops quickly by one order of magnitude during the experiment. Meanwhile, F_{Ca} remains almost constant for FRAC1. The drop is about 8 times faster for FRAC3 than for FRAC2 (Fig. 5c). The effluent pH follows the temporal trends of calcium concentration and flux (Fig. 5a,b,c).

Evolution of the effluent fluid chemistry for FRAC2 and FRAC3 is directly linked to the main channel breakthrough and subsequent flow localization, while fluid chemistry remains constant for FRAC1 because the conical channels remained very small and localized near the sample inlet.

3.1.3. Dissolution rates

As summarized in Table 4, the initial dissolution rates (r_0) for FRAC2 and FRAC3 are about 52 and 114 times higher than for FRAC1, respectively. The dissolution rates for FRAC2 and FRAC3 decrease quickly, but remain on average ($\bar{r}_c$) about 14 and 29 times higher than for FRAC1, respectively. The rate of channel growth $\bar{r}_w$ in FRAC2 remains close to the initial dissolution rate (6.94 vs 7.22 $\mu m \cdot h^{-1}$), whereas it is noticeably lower than r_0 for FRAC3 (8.95 *vs* 15.95 $\mu m \cdot h^{-1}$). The maximum rate of channel growth, $\bar{r}_{w-max}$, is 11.14 and 16.15 $\mu m \cdot h^{-1}$ for FRAC2 and FRAC3, respectively.

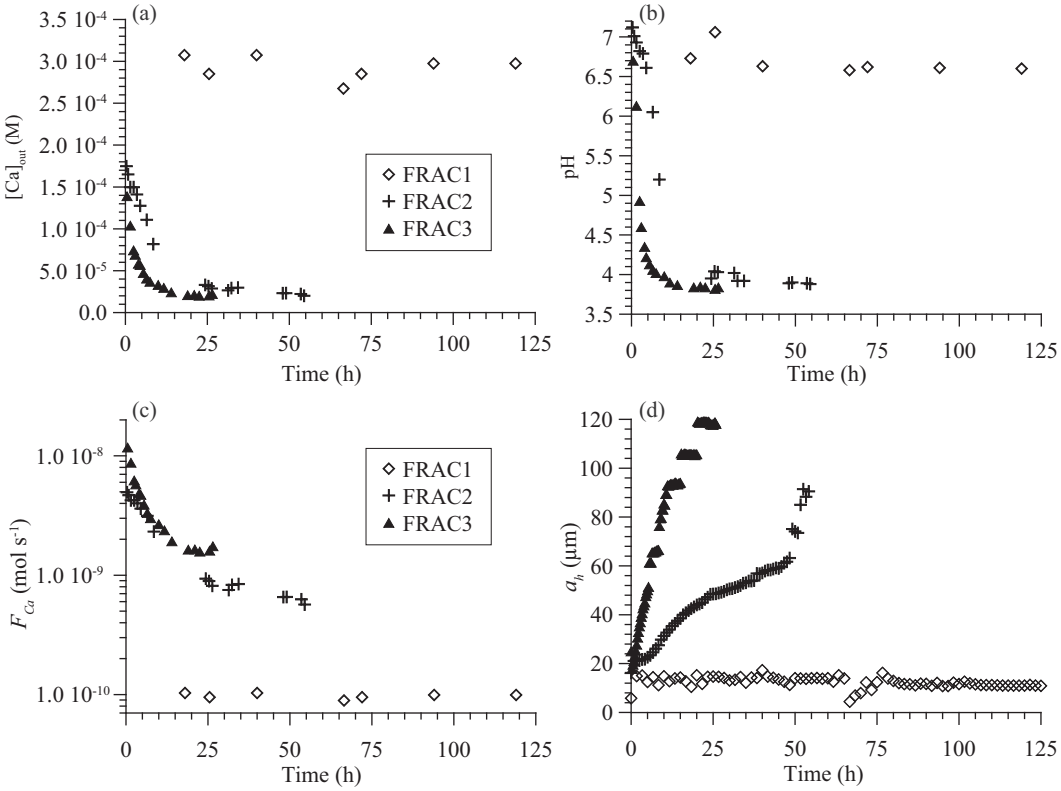

Fig. 5. (a) Effluent calcium concentration ($[Ca]_{out}$), (b) effluent pH, and (c) flux of Ca (F_{Ca}) at the outlet of the samples; and (d) hydraulic aperture (a_h) changes during the flow-through experiments.

Table 4
Dissolution rates for the three fractured samples.

Sample	Initial dissolution rate r_0 (µm·h^{-1})	Average dissolution rate $\bar{r}_c$ (µm·h^{-1})	Average dissolution rate of the main channel $\bar{r}_w$ (µm·h^{-1})	Maximum local dissolution rate within the main channel $\bar{r}_{w-max}$ (µm·h^{-1})
FRAC1	0.14	0.14	–	–
FRAC2	7.22	2.11	6.94	11.14
FRAC3	15.95	4.23	8.95	16.15

3.1.4. Flow and permeability evolution

Initially, the Péclet number, Pe_0, is 7, 598, and 1648 for FRAC1 to FRAC3, respectively (Table 1). The distribution of the initial fluid velocity, $\bar{v}_0$, is expected to be uniform in the fracture plane and is proportional to the experimental flow rate (Table 1).

The changes in hydraulic aperture calculated from pressure measurements are presented in Fig. 5d. At the lowest flow rate (FRAC1, 1.2 cm^3·h^{-1}), while dissolution of calcite promotes the increase of the fracture aperture near the inlet, clays were not removed by the fluid and remained fixed on the fracture walls, explaining why the hydraulic aperture decreased slightly during the experiment, from 14 to 11 µm. At the intermediate flow rate (FRAC2, 102 cm^3·h^{-1}), a_h increases nonlinearly (Fig. 5d), from 21 to 90 µm. At the highest flow rate (FRAC3, 300 cm^3·h^{-1}), the increase of a_h is more linear, from 15 to 120 µm. It is worth noting that the hydraulic aperture increases exponentially towards the end of the experiments for FRAC2 and FRAC3. As the pressure difference approaches the detection limit of the pressure sensors, large uncertainties may be expected, which may explain the large differences between a_h and a_{h-sim} (Table 4).

Using the post-reaction fracture geometry, flow modeling was performed to evaluate the changes in fluid velocity distribution (Fig. 6). The dissolution in FRAC1 does not cause significant changes in the average fluid velocity ($\bar{v}$) and fluid velocity distribution (Fig. 6b) because of the localization of the dissolution near the sample inlet. In contrast, the fluid velocity decreases by about one order of magnitude during the experiment for FRAC2 and FRAC3. In addition, the velocity varies over several orders of magnitude (Fig. 6b), with high flow velocities within the main channels and low flow velocities confined in areas progressively inaccessible to the fluid as the dissolution progresses (Fig. 6a).

3.1.5. Relationship between different types of aperture

The measurements of a_c and a_m are in good agreement, but are different from hydraulic apertures inferred from the differential pressure measurements (a_h) or from the flow simulations of the post-experiment aperture fields (a_{h-sim}) (Table 4). The observed differences between a_h and a_m (or a_c) can be explained by the combined effects of clay spots and the development of heterogeneous flowpaths. For FRAC1, the channel did not break through, and the peak position of the aperture distribution remains close to the initial aperture a_0 (Fig. 3b). Because dissolution is restricted to the inlet of the fracture, the hydraulic aperture does not change noticeably over time. In addition, some clay particles that became loosely positioned in the fracture void due to the dissolution of surrounding calcite (Fig. 4a) may have contributed to a small decrease of a_h. For FRAC2 and FRAC3, the fluid velocity is sufficiently high to transport clay particles that were released after calcite dissolution (Fig. 4b,c), and the rapid increase of a_h is dominated by the growth of the channels. While the absolute hydraulic aperture values are not directly comparable because of the difference in flow rate and the duration of the experiment, the ratio between hydraulic and mechanical aperture provides insights regarding the development of the channels.

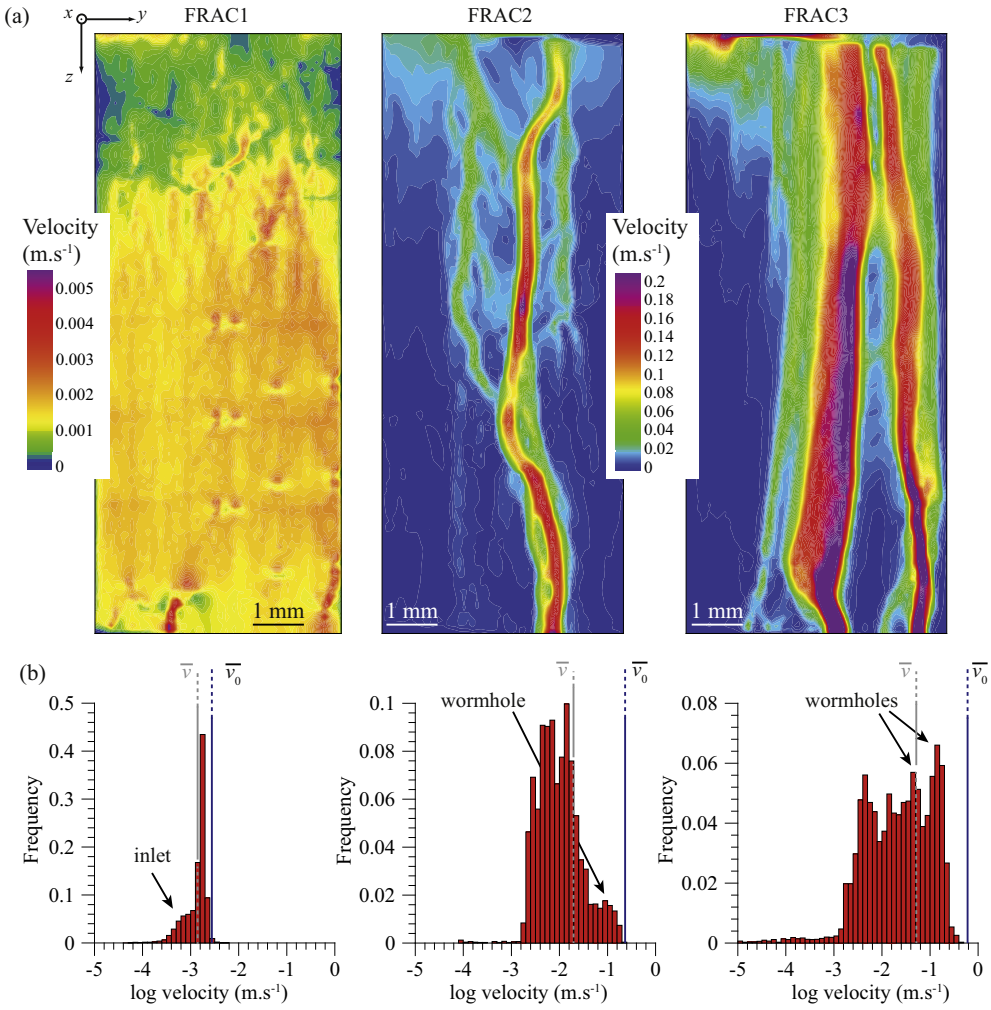

Fig. 6. (a) Flow field (simulated) in the fractures after the experiments for FRAC1, FRAC2, and FRAC3; and (b) corresponding histograms of velocity; the initial velocity ($\bar{v}_0$) and average velocity ($\bar{v}$) are mentioned in the figure.

3.2. Reactive transport modeling results

3.2.1. Effects of calcite reactivity

For the range of kinetic rates (FRAC1–3_sim_k_1*) and surface roughness factors (FRAC1–3_sim_SFR*) tested in the simulations, we observed different dissolution patterns.

Using logk_1 of −0.05 (Chou et al., 1989) in the kinetic formulation, the predicted fracture dissolution patterns at the different flow rates are consistent with the experimental observations. Dissolution is predicted to be localized at the inlet at the low flow rate (FRAC1_sim_k_1-Chou), whereas channels are created at the high flow rates (FRAC2_sim_k_1-Chou and FRAC3_sim_k_1-Chou). A single channel penetrates the fracture at 102 $cm^3 \cdot h^{-1}$, and the channels at 300 $cm^3 \cdot h^{-1}$ are highly ramified (Fig. 7a). Overall, average aperture decreases along the flow direction, indicating the decrease in dissolution rate, which is caused by the increase in pH and saturation state along the flow direction.

The dissolution of calcite leads to an increase in the fracture volume and hydraulic aperture. The mechanical aperture and hydraulic aperture are 38 and 25 μm for FRAC1_sim_k_1-Chou (t_i = 164.5 h), respectively. They reach 292 μm and 266 μm for FRAC2_sim_k_1-Chou (t_i = 55 h), and 386 μm and 166 μm for FRAC3_sim_k_1-Chou (t_i = 26.5 h), respectively.

Overtime, the effluent Ca concentration shows decreasing trends at the higher flow rates, from 1.26 10^{-4} M to 0.91 10^{-4} M for FRAC2_sim_k_1-Chou, and from 1.12 10^{-4} M to 1.07 10^{-4} M for FRAC3_sim_k_1-Chou; whereas at the low flow rate (FRAC1_sim_k_1-Chou), the effluent concentration is about 2.2 10^{-4} M throughout the simulation (Fig. 7f). F_{Ca} shows similar temporal trends as $[Ca]_{out}$. The effluent pH also shows decreasing trend at the high flow rates, from 5.6 to 4.4 for FRAC2_sim_k_1-Chou, and from 5.0 to 4.7 for FRAC3_sim_k_1-Chou. The effluent chemistry indicates a decrease in the overall calcite dissolution rate over time at the higher flow rates.

The other kinetic coefficients for calcite dissolution reported in the literature are smaller, log k_1 is −0.3 in Plummer et al. (1978) and −1.08 in Deng et al. (2015). Accordingly, for these simulations, the dissolution rate in the fracture at any given flow rate, as indicated by the effluent Ca concentration and Ca flux, is lower. For example, the initial $[Ca]_{out}$ is about 2 10^{-4} M for the simulation using log k_1 of −0.3 at 1.2 $cm^3 \cdot h^{-1}$ (FRAC1_sim_k_1-Plummer), whereas it is about 1.6 10^{-4} M for the simulation that uses log k_1 of −1.08 (FRAC1_sim_k_1-Deng). Using the smaller kinetic coefficients also leads to shifts in the spatial patterns of calcite dissolution, i.e., channel development at the higher flow rates is suppressed (Fig. 7b,c). Channels for FRAC2_sim_k_1-Plummer are ramified and no channel is observed for FRAC3_sim_k_1-Plummer. The effluent Ca concentration, Ca flux and effluent pH decrease over time for FRAC2_sim_k_1-Plummer, but to a lesser extent than FRAC2_sim_k_1-Chou, and do not change observably for FRAC3_sim_k_1-Plummer. For simulations using log k_1 of −1.08, the dissolution patterns are uniform at the two higher flow rates (FRAC2_sim_k_1-Deng & FRAC3_sim_k_1-Deng, Fig. 7c). As a result, the effluent chemistry does not change over time (Fig. 7f, g).

Reaction rate is also affected by the reactive surface area (Eq. (14)),

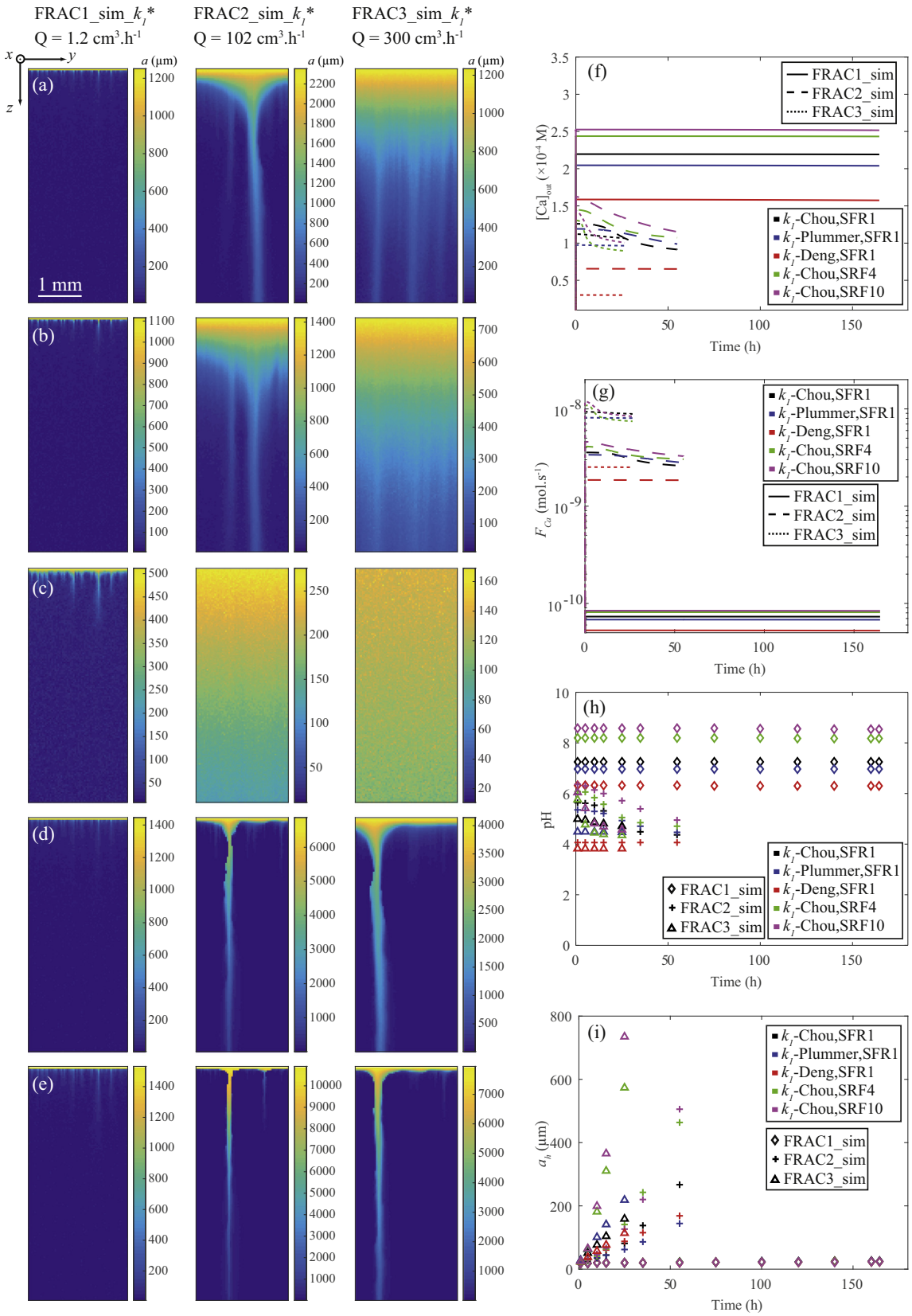

Fig. 7. Modeling results exploring the role of reaction rates on the dissolution pattern for FRAC1–3_sim_k_1* and FRAC1–3_sim_SFR*. (a)–(c) Final aperture maps from simulations that uses log $k_1 = -0.05$ (Chou et al., 1989) (FRAC1–3_sim_k_1-Chou), log $k_1 = -0.3$ (Plummer et al., 1978) (FRAC1–3_sim_k_1-Plummer), and log $k_1 = -1.08$ (Deng et al., 2015) (FRAC1–3_sim_k_1-Deng), respectively; SFR = 1 in these simulations; (d)–(e) final aperture maps from simulations that use SRF = 4 and 10 (FRAC1–3_sim_SRF4 and FRAC1–3_sim_SRF10), respectively. Corresponding temporal evolutions of (f) effluent Ca concentration, (g) Ca flux, (h) effluent pH, and (i) hydraulic aperture a_h.

which is typically an even more poorly constrained parameter than the kinetic coefficient. Simulations that use log k_1 of −0.05 and assume various levels of surface roughness (FRAC1–3_sim_SRF4/10) show effluent chemistry and dissolution patterns that differ from the simulations that use the same kinetic coefficient but without surface roughness, i.e., SFR = 1 (FRAC1–3_sim_k_1-Chou). Assuming a SRF of 4 (Fig. 7d), i.e., increasing the reactive surface area by a factor of four compared to the geometric surface area (Eq. (15)), results in an increase in the overall dissolution rate in the fracture (Fig. 7g). For example, initial $[Ca]_{out}$ for FRAC1_sim_SRF4 is 2.44 10^{-4} M, 11% higher than that of FRAC1_sim_k_1-Chou. This increase is by a small percentage compared to the SRF because of reduced local thermodynamic driving force. At the higher flow rates, stronger channelization is observed. The decrease in the overall calcite dissolution rate is therefore more substantial. For FRAC3_sim_SRF4, $[Ca]_{out}$ decreases from 1.3 10^{-4} M to 0.9 10^{-4} M. Further increase in the roughness factor (e.g. FRAC3_sim_SRF10) results (Fig. 7d) in stronger channelization and slightly higher effluent Ca concentrations (Fig. 7f).

Comparing the simulation results with the experimental observations, log k_1 of −0.05 and SRF of 4 provides a reasonable agreement with both the dissolution patterns and initial effluent chemistry, and are therefore used in the simulations that will be discussed below. Simulations using these parameters, however, show a flatter decreasing trend in the effluent chemistry at the high flow rates than was observed in the experiments. The effluent Ca concentration is predicted to decrease by 26% (from 1.5 10^{-4} M to 1.1 10^{-4} M) for FRAC2_sim_SRF4, and by 30% (from 1.3 10^{-4} M to 0.9 10^{-4} M) for FRAC3_sim_SRF4 by the end of the simulations, whereas the reductions observed in the experiments are 88% and 87%, respectively.

As a result, the high flow rates simulations over-estimated the cumulative calcite dissolved, which can be measured by the time integral of the Ca flux, and thus the fracture volume change due to calcite dissolution. The mechanical aperture at the end of the simulations is 325 and 356 μm for FRAC2_sim_SRF4 and FRAC3_sim_SRF4, respectively. The hydraulic apertures by the end of the simulations, 464 and 613 μm for FRAC2_sim_SRF4 and FRAC3_sim_SRF4, respectively, are also higher than what were estimated based on the flow simulations using the reacted fracture geometries from the experiment at the corresponding flow rates, i.e. 183 and 171 μm. The rapid increase in the hydraulic apertures over time is caused by channelization in the fractures.

As indicated by the simulation results above, the extent of the discrepancy can hardly be explained by the expected variations in the kinetic coefficient or surface roughness. This implies that the decrease in effective surface area due to flow channeling in the fracture plane, which was accounted for in the simulations, is not the only mechanism that causes the reaction rate to decrease in the experiments. In the following sections, we investigate the effects of mineral spatial heterogeneity and transport limitation across the fracture aperture on the reaction rate.

3.2.2. Effects of mineral spatial heterogeneity

The presence of mineral heterogeneity does not affect the dissolution regime. For the range of mineral heterogeneity tested in the simulations (FRAC1–3_sim_MH*), the dissolution patterns switch from compact dissolution to channelization as flow rate increases. Accordingly, the effluent pH, $[Ca]_{out}$, and F_{Ca} from the low flow rate simulations show no temporal change, whereas the effluent chemistry displays a clear decreasing trend in the high flow rate simulations (Fig. 8).

Mineral heterogeneity, however, has a clear impact on the dissolution patterns, i.e., the location and morphology of the channels. The channels tend to develop where the clay spots, i.e. high porosity zones, are present. For example, in the simulations that assume clustered distribution of the clays, the channels switch from right to left with the clay spots (Fig. 8a,b,c, FRAC2/3_sim_MH-c1 to FRAC2/3_sim_MH-c3). For FRAC2/3_sim_MH-b, both the primary and secondary channels coincide with the clay layers (Fig. 8d). This is because at the clay spots, fracture surface retreats at a higher rate, resulting in a stronger local feedback with the flow rate.

For all simulations with mineral heterogeneity, the temporal evolution of effluent chemistry is similar (Fig. 8e,g), and comparable to the simulations without mineral heterogeneity (Fig. 7d). This is because the clay spots only account for a small fraction of the fracture surface area. However, unlike the mechanical aperture, the hydraulic aperture shows substantial variations (Fig. 8h). For example, the hydraulic aperture ranges from 358 to 599 μm for FRAC2_sim_MH*, and from 603 to 742 μm for FRAC3_sim_MH*. High spatial correlation in the clay spots, such as the banded distribution, tends to promote channelization and result in a larger increase in the hydraulic aperture.

The simulations imply that although the presence of a small fraction of mineral heterogeneity does not affect the overall evolution of geochemical reactions, it can have a substantial impact on fracture morphology and the resulting hydraulic aperture changes.

3.2.3. Effects of transport limitation across the fracture aperture

The simulations that account for the transport limitation across the fracture aperture due to the diffusive boundary layer (Fig. 9, FRAC1–3_sim_DBL) show fracture evolution that is different from the corresponding simulations that do not consider the transport limitation (Fig. 7, FRAC1–3_sim_SRF4).

Although the location of the channels that develop at the higher flow rates is not affected, the morphology of the channels changes noticeably. The downstream apertures in the channels are more comparable to the upstream values (Fig. 9a). This indicates that although the dissolution rate in the channel at the upstream is lowered due to the transport limitation across the fracture aperture, dissolution in the channel at the downstream is promoted because fluid reactivity is maintained. Consequently, the hydraulic aperture of the fracture increases more substantially, reaching 647 and 532 μm for FRAC2_sim_DBL and FRAC3_sim_DBL, respectively. Both values are significantly higher than the corresponding mechanical aperture, i.e., 268 and 282 μm (Fig. 9e), indicating strong fracture channelization.

As a result of the strong channelization and transport limitation across the fracture aperture, the overall calcite dissolution rate is further reduced over time. The effluent Ca concentration is reduced by 54% to 6.8 10^{-5} M for FRAC2_sim_DBL, and by 59% to 5.3 10^{-5} M for FRAC3_sim_DBL (Fig. 9b). Similarly, the extent of decrease in Ca flux and pH is more evident (Fig. 9c,d). Consequently, the mechanical apertures at the end of the simulations (reported above) are smaller than the previous simulations without transport limitation across the fracture aperture.

The simulation results indicate that the transport limitation across the fracture aperture in the channels is another mechanism that further reduces the overall dissolution rate and therefore affects fracture evolution.

3.2.4. Evolution of the dissolution rates

The simulations showed that not only the overall dissolution rate in the fracture decreases over time, as indicated by the decreasing trends in the Ca fluxes, the spatial distribution of calcite dissolution rate in the fractures varies over time as well due to continuous fracture geometry evolution. Fig. 10 shows the histograms of local dissolution rate at multiple time steps of FRAC2_sim_DBL. Initially, the high reaction rates are localized at the inlet. When the channel starts to form, local dissolution rates increase slightly in the channel, while local dissolution rates decrease considerably in the non-channelized regions. A clear bimodal distribution is observed for local dissolution rates. As the channel develops further, although the dissolution rate distribution remains bimodal, the local dissolution rates in the channels decrease due to the diffusion limitation across the fracture aperture, except at the front of the channel. Thus, the high dissolution rate peak shifts towards

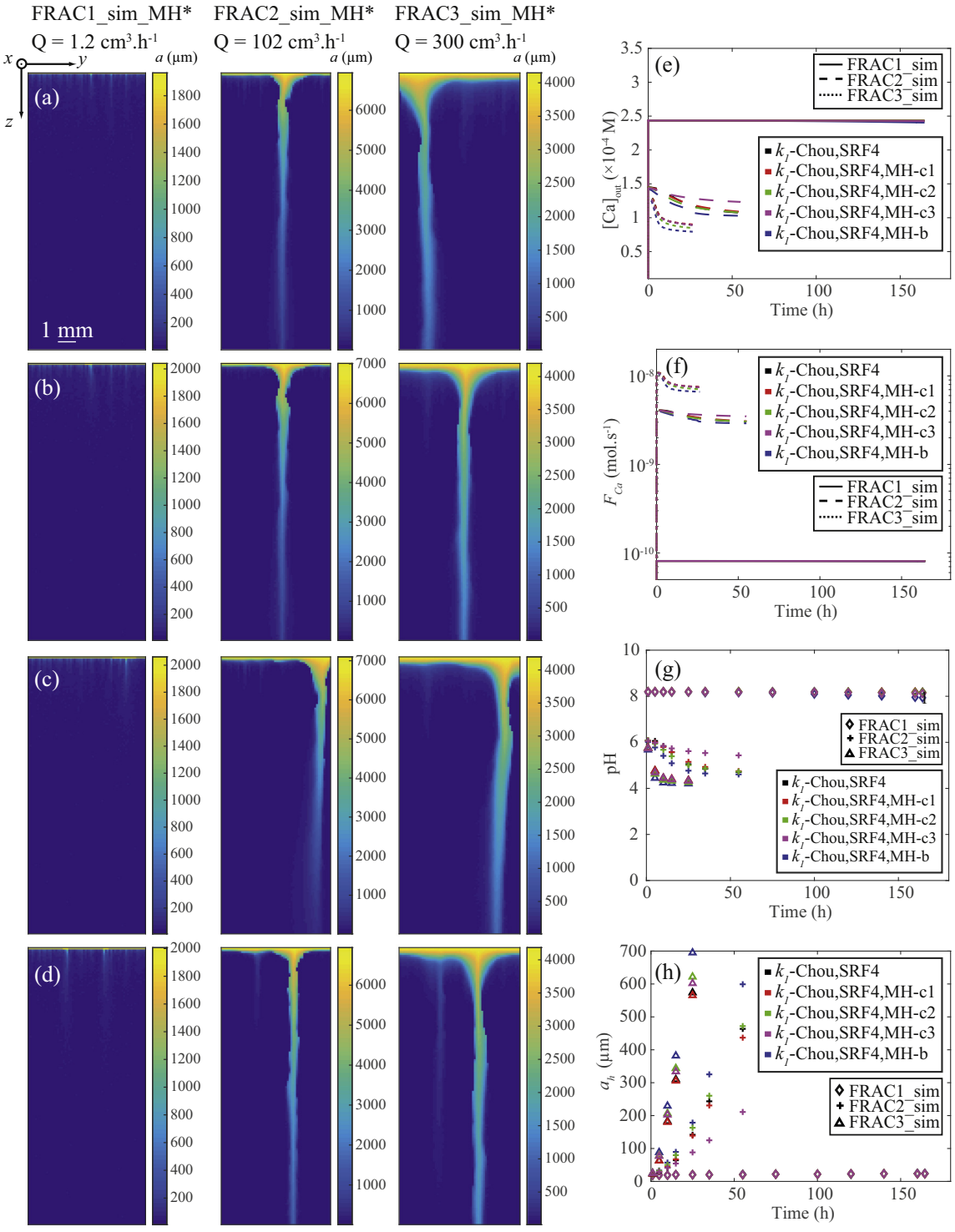

Fig. 8. Modeling results exploring the role of mineral heterogeneity on the dissolution pattern of FRAC1–3_sim_MH*. (a–d) Aperture maps at the end of the simulation that uses log $k_1 = -0.05$ (Chou et al., 1989) and SRF = 4 with mineral heterogeneity that corresponds to the mineral masks shown in Fig. 2. Temporal evolution of (e) effluent Ca concentration, (f) Ca flux, (g) effluent pH and (h) hydraulic aperture.

the lower value.

4. Discussion

4.1. Effects of mineralogical spatial heterogeneity on the wormhole development

Although it was not possible to precisely quantify and locate the clay spots and/or clay layers prior to the experiments, the impacts of clays on the evolution of fracture geometry and fluid flow are evident.

Modeling with mineral spatial heterogeneity has shown that even though clays -or more generally any mineral phases of different reactivity from the dominant primary mineral- account for a small percentage of the fracture surface and do not alter overall geochemical evolution substantially, they can significantly affect the morphology of the channels that form. Channelization is sensitive to small scale

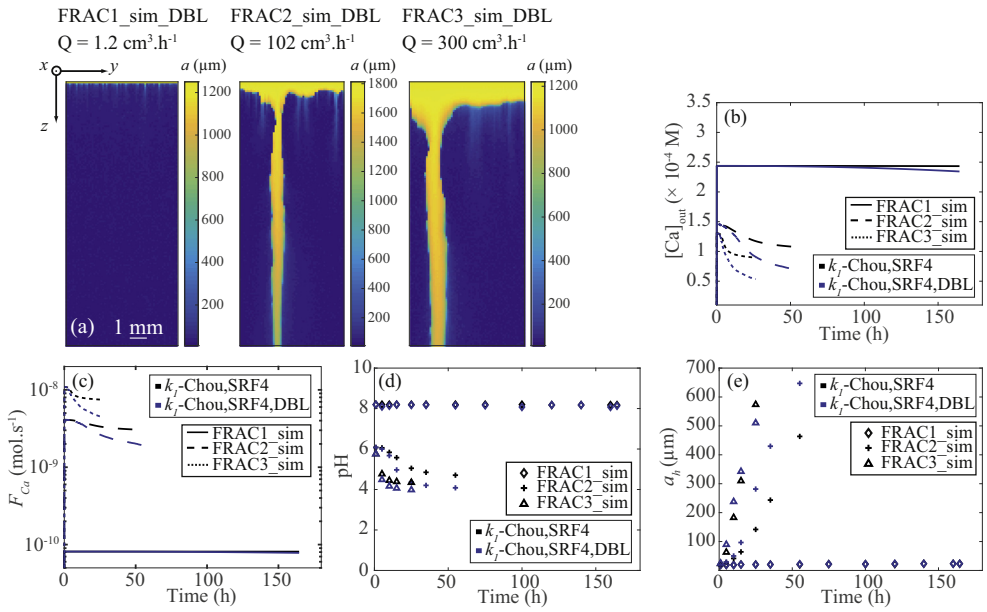

Fig. 9. Modeling results exploring the role of transport limitation across the fracture aperture on the dissolution pattern for FRAC1–3_sim_DBL. (a) Aperture maps at the end of the simulation that uses log $k_1 = -0.05$ (Chou et al., 1989) and SRF = 4 with transport limitation across fracture walls. Temporal evolution of (b) effluent Ca concentration, (c) Ca flux, (d) effluent pH and (e) hydraulic aperture.

mineral spatial heterogeneity because it is a result of the positive feedback between reaction and flow that magnifies local perturbations. Perturbations are typically initiated by geometry and flow heterogeneity, and can also be caused by mineral heterogeneity. Fracture hydraulic properties, which are highly dependent on the morphology of the channels, are therefore largely modified by the presence of mineral spatial heterogeneity. For example, if the clays follow patterns with high spatial connectivity (e.g., MH-b), the development of channels is promoted, resulting in a considerable increase in fracture hydraulic aperture. However, the modeling results show that the dissolution regime is not influenced by the presence of small spatial heterogeneity.

The impacts of clays on fracture evolution are dependent on flow rate. At the low flow rate (FRAC1), the reorganization of the clay particles (Fig. 4a) contributed to the decrease in hydraulic aperture (Fig. 5d). Even though reactions or channeling were not affected during the experiment of FRAC1 as demonstrated by the constant effluent chemistry (Fig. 5a), remaining clays on fracture surfaces could influence fracture evolution by increasing the characteristic time of transverse diffusion through the clay layer compared to advection in the fracture void (Chen et al., 2014; Deng et al., 2016; Noiriel et al., 2007b). In contrast, at high flow rates (FRAC2 and FRAC3), the clay particles detached from the fracture surface and were flushed out of the fracture, as no evidence of clays was found in the fracture void (Fig. 4b,c). In these cases, dissolution patterns are clearly influenced by local clay spots (Fig. 3), as the loss of clays can trigger instabilities in the dissolution front.

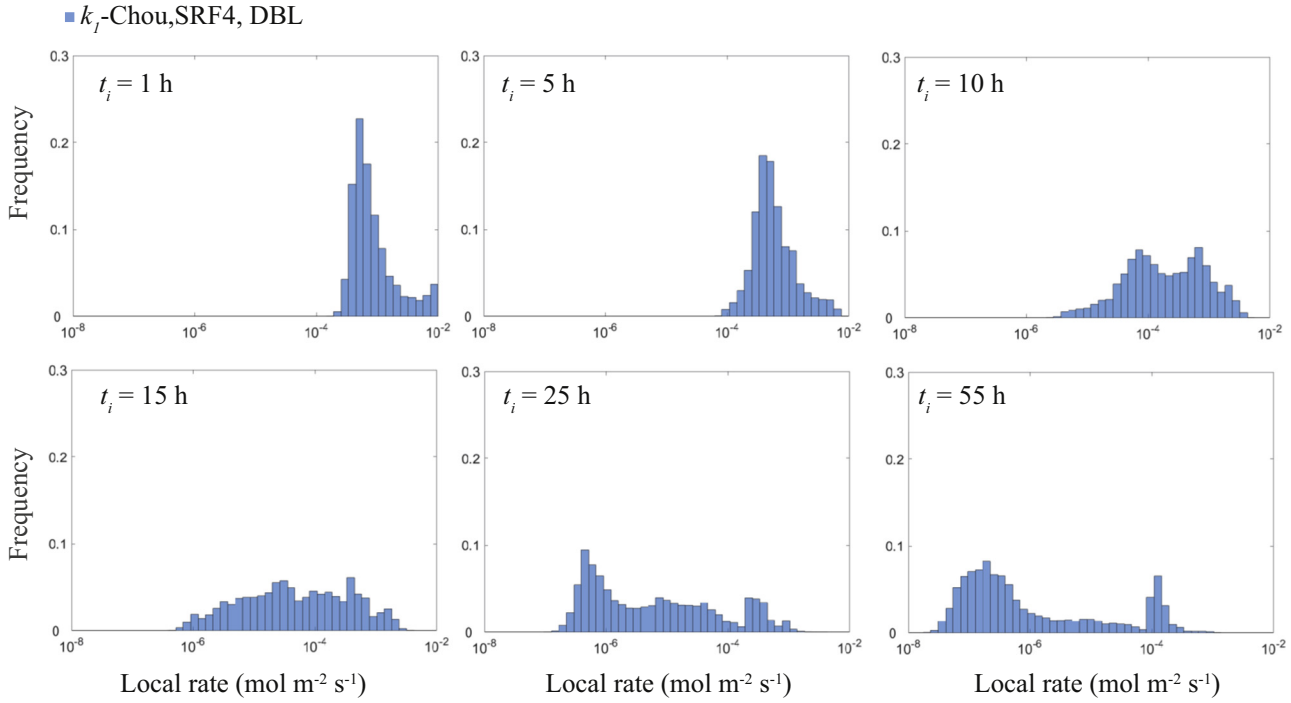

Fig. 10. Distribution of local dissolution rates for FRAC2_sim_DBL at different simulation times. The evolution of the growth rate of the main channel is clearly visible in the corresponding histograms.

4.2. Dissolution process and channel formation

In these experiments at high *Da*, we observe the transition from conical wormhole to dominant wormhole and to ramified wormhole by simply increasing *Pe*. The modeling results also pointed out that the dissolution regime is very sensitive to the calcite dissolution rate and thus the *Da* number. However, large uncertainties exist in the kinetic constants that are used to calculate *Da* or in modeling. For example, k_1 values reported in different studies vary by a factor of ~10 (e.g., Alkattan et al., 1998; Chou et al., 1989; Plummer et al., 1978). This is partly because the surface reaction rate is a difficult parameter to determine. For example, at pH below 4–5, calcite dissolution rate is limited by transport in a boundary layer. Conditions of the experimental techniques commonly used to determine surface reaction rates, e.g., rotating disc experiments, may not be directly comparable and transferrable to flow-through experiments and simulations. Thus, the uncertainty in the surface dissolution rate is among the primary sources of uncertainties for modeling reactive transport.

The impact of the kinetic rate path on the dissolution regime has also been pointed out by Noiriel (2015), based on observations from two sets of fracture experiments. Injecting fluid with the same initial pH in limestone fractures at similar initial *Pe* and *Da* numbers, but using a strong acid (HCl) in one experiment and a weak acid (H_2CO_3) in the other led to different dissolution regimes.

4.3. Impact of local transport regime on the feedback between chemistry and transport

The experimental results for FRAC2 and FRAC3 indicate a considerable decrease in the overall calcite dissolution rate during the experiments.

Reduction of reactive surface area is often incorrectly used to explain reduction in overall reaction rate during flow-through experiments when in fact the reduction is caused by changes in the close coupling between chemical reactions and transport processes at the pore-scale (Noiriel and Daval, 2017). While the reactive surface area in a fracture may change as the roughness of fracture walls is modified or when minerals with a different reactivity are present at the fracture walls, the extent of the resulting surface area change in the experiments is, in many cases, insufficient to explain the changes in the reaction rate.

In contrast, changes in fluid velocity and in transverse diffusion in the vicinity of the fluid-mineral interface, or across fracture aperture, are likely to influence the close coupling between chemical reactions and transport. Strong transport limitations can arise from (i) diffusion limitations caused by a growing altered layer (Deng et al., 2017; Noiriel et al., 2007b), or (ii) diffusive boundary layer in the fluid due to substantial aperture enlargement associated with flow channeling (Deng et al., 2015; Deng et al., 2016). In our study, as revealed by XMT, no altered micro-porous matrix was observed in experiments FRAC2 and FRAC3, but flow channeling is evident.

Fig. 11 provides a conceptual illustration of the cross-aperture transport processes at the beginning of the experiment and after the channels have developed. Initially, well-mixed conditions can be assumed across the fracture aperture. As pointed out in Li et al. (2008), two necessary conditions need to be satisfied for a concentration gradient across the aperture to develop: (i) comparable advection and reaction rates, and (ii) faster reaction rate than transverse diffusion. Although under the strong acidic conditions of the experiments, the reaction rate is larger than the diffusion rate, and the transfer of reactants and products to/from the fracture surfaces is limiting, the velocities in the initial fractures are high and advection is dominant (Fig. 6). This is also consistent with the results of Li et al. (2008), which showed negligible concentration gradients in 10 μm pores in the velocity range of 10^{-2}–10^{-1} m·s^{-1}, conditions comparable to those during the beginning of the experiments.

Once a channel breaks through the fracture, it serves as the major flow conduit. The velocity field becomes heterogeneous, with the fluid velocity decreasing more substantially in the non-channelized fracture void (by one to three orders of magnitude) as compared to the main channel (Fig. 6). While the flow remains advective in the main channel, flow in the rest of the fracture decreases, thus increasing the importance of diffusive transport in the low-aperture fracture voids. In contrast, transport in the main channel couples advection in the flow direction with transverse diffusion of the reactant/products across the channel. As the diameter of the channel increases, the diffusive length between the fracture walls in the flow path increases (Molins et al., 2012), leading to the poorly-mixed conditions as described by Li et al. (2008). Due to incomplete transverse mixing, Li et al. (2008) have observed large discrepancy in the effective dissolution rate of calcite between a fracture represented by a Poiseuille flow and a fracture within which complete mixing is assumed at average fluid velocities between 10^{-3} and 10^{1} m·s^{-1}. These values are comparable to the velocities in the reacted channels in the experiments (10^{-3}–10^{-1} m·s^{-1}) (Fig. 6). The scaling effect on the dissolution rate may also increase as the channels grow. As observed by Li et al. (2008), the scaling effect was about 6 times larger in 1000 μm pores than the 10 μm pores at flow velocities in the range 10^{-2}–10^{-1} m·s^{-1}.

The experimental and simulation results indicate that channelization affects overall mineral reaction in the fracture through two mechanisms. Channelization reduces advective transport and fluid-mineral contact in the regions within which flow decreases. In addition, channelization leads to larger apertures, in which case the diffusion limitation across the fracture aperture becomes important and transverse concentration gradients develop.

The changes in these transport processes within fractures FRAC2 and FRAC3 can explain why no positive feedback sensu stricto was observed throughout the experiment. A positive feedback loop between chemistry and transport, which is often mentioned during channelization processes, would result in increasing growth rate of the main channel at the expense of the whole fracture void. In the experiment, the average growth rate of the main channel, $\bar{r}_w$, remains equal (FRAC2) or smaller (FRAC3) than the overall initial fracture opening rate (Table 4). The simulations (FRAC2/3_sim_DBL) confirmed the decrease of the growth rate of the channel after being well established, and also showed a small degree of enhancement of the channel growth rates during initial fluid localization (Fig. 10). The same process might have occurred during the experiments. Unfortunately, no intermediate 3D data set of the fractures was available to confirm this modeling observation. Nevertheless, the so-called positive feedback is likely to be a transient process, with the local dissolution rates in the channels increasing at the beginning of flow channeling, but decreasing progressively thereafter due to changes in the fluid velocity and diffusion limitations across the fracture aperture.

5. Conclusions

We have presented an experimental and modeling study that investigates the impact of flow rate, mineral spatial heterogeneity, and transport limitation across the fracture aperture on the dissolution regimes in planar limestone fractures. Although the fractures have planar and smooth geometries, channelization associated with different dissolution regimes were observed, from conical wormhole (FRAC1), to dominant wormhole (FRAC2) and ramified wormhole (FRAC3) with increasing flow rate. At the higher flow rates, i.e., 102 and 300 cm^3·h^{-1}, the growth of the channels is associated with a rapid increase in hydraulic aperture but a decrease in reactivity.

Simulations exploring variations in dissolution rate, mineral spatial heterogeneity and transport limitation across the fracture aperture were used to decipher the mechanisms involved in channel development and the resulting reduction of reactivity observed during the experiments. Overall, the simulations captured the changes in the fracture

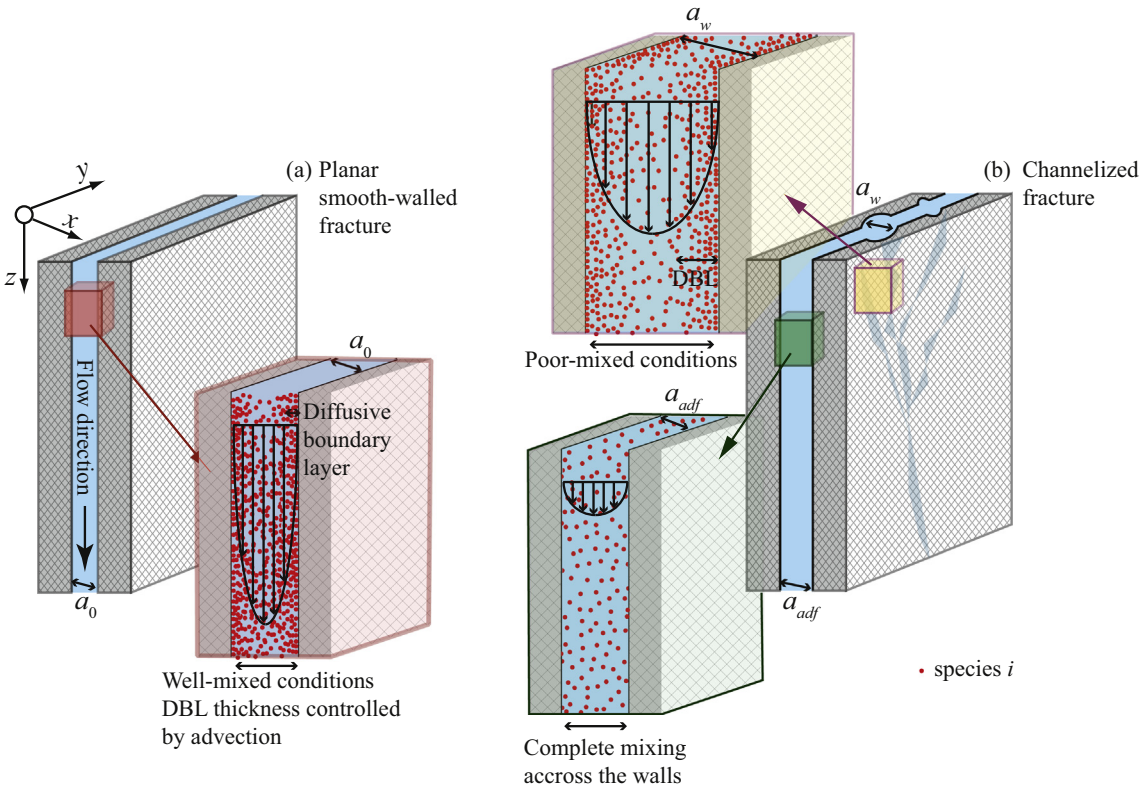

Fig. 11. Sketch of the local transport process changes in a fracture during channel formation. (a) Well-mixed conditions in highly advective initial planar fracture; (b) channelized fracture with fluid velocity and transport reduction in the area progressively inaccessible to the fluid (whose aperture is a_{adf}) where complete mixing across the fracture aperture is assumed, and poor-mixed conditions in growing channel (whose aperture is a_w).

dissolution regimes, and confirmed the controls of the Péclet number on the fracture evolution patterns. The simulations that assume different kinetic coefficients or reactive surface areas also point to the role of the Damköhler number in influencing the fracture geometry evolution.

The morphology of the channels is sensitive to any potential mineral spatial heterogeneity, although the dissolution regime is not affected. The simulations also showed that a transport limitation across the fracture aperture due to strong channelization is another mechanism that causes the increasingly limited calcite dissolution.

Overall, the 2.5D model was able to capture the major observations in the experiments. Quantitative differences between the modeling results and the experimental observations, especially in hydraulic apertures, remain. The differences may be caused by the fact that initial fracture geometries and spatial distribution of clay spots were not available for the setup of the model. They may also be attributed to the assumptions of the 2.5D model. For example, the 2.5D model calculates the flow field and hydraulic properties using the depth-averaged Reynolds equation, which tends to over-estimate flow. Not being able to fully capture some local flow phenomena may also explain why the simulations failed to reproduce the strong ramification of channels observed in experiment FRAC3. In addition, the treatment of the diffusion limitation due to the boundary layer is highly simplified. Nevertheless, the 2.5D model remains a useful and computationally efficient tool for investigating the interplay between flow, transport and reactions in fractures, especially fractures in multi-mineral systems. Comparisons with a full 3D treatment of the fractures are needed to better understand the exact conditions under which the 2.5D model may be insufficient.

Acknowledgments

Hand Deng was supported by the Center for Nanoscale Controls on Geologic CO_2 (NCGC), an Energy Frontier Research Center funded by the U.S. Department of Energy, Office of Science, Basic Energy Sciences under Award # DE-AC02-05CH11231. Catherine Noiriel is grateful to Philippe Gouze and Benoît Madé for their advice and assistance in the performance of the experiments at University of Montpellier, laboratoire Géosciences. 3D imaging was performed at the European Synchrotron Radiation Facility, beamline BM05, under proposal ME920; this work was also supported by the Institute Carnot ISIFOR through Project SEQFRAC-450043. The authors would also like to thank Dr. Carl Steefel for the discussions.

References

Alkattan, M., Oelkers, E.H., Dandurand, J.-L., Schott, J., 1998. An experimental study of calcite and limestone dissolution rates as a function of pH from −1 to 3 and temperature from 25 to 80 °C. Chem. Geol. 151, 199–214.

Andreani, M., Luquot, L., Gouze, P., Godard, M., Hoise, E., Gibert, B., 2009. Experimental study of carbon sequestration reactions controlled by the percolation of CO_2-rich brine through peridotites. Environ. Sci. Technol. 43, 1226–1231.

Aydin, A., 2000. Fractures, faults, and hydrocarbon entrapment, migration and flow. Mar. Pet. Geol. 17, 797–814.

Bazin, B., 2001. From matrix acidizing to acid fracturing: a laboratory evaluation of acid/rock interactions. SPE Prod. Facil. 16, 22–29.

Chen, L., Kang, Q., Viswanathan, H.S., Tao, W.-Q., 2014. Pore-scale study of dissolution-induced changes in hydrologic properties of rocks with binary minerals. Water Resour. Res. 50, 9343–9365.

Cheung, W., Rajaram, H., 2002. Dissolution finger growth in variable aperture fractures: role of the tip-region flow field. Geophys. Res. Lett. 29, 2075. https://doi.org/10.1029/2002GL015196.

Chou, L., Garrels, R.M., Wollast, R., 1989. Comparative study of the kinetics and mechanisms of dissolution of carbonate minerals. Chem. Geol. 78, 269–282.

Daccord, G., Lietard, O., Lenormand, R., 1993. Chemical dissolution of a porous medium by a reactive fluid: 1. Model for the wormholing phenomenon. Chem. Eng. Sci. 48, 169–178.

Deng, H., Fitts, J.P., Crandall, D., McIntyre, D., Peters, C.A., 2015. Alterations of fractures in carbonate rocks by CO_2-acidified brines. Environ. Sci. Technol. 49, 10226–10234.

Deng, H., Molins, S., Steefel, C., DePaolo, D., Voltolini, M., Yang, L., Ajo-Franklin, J., 2016. A 2.5D reactive transport model for fracture alteration simulation. Environ. Sci.

Technol. 50, 7564–7571.
Deng, H., Voltolini, M., Molins, S., Steefel, C., DePaolo, D., Ajo-Franklin, J., Yang, L., 2017. Alteration and erosion of rock matrix bordering a carbonate-rich shale fracture. Environ. Sci. Technol. 51, 8861–8868.
Deng, H., Steefel, C., Molins, S., DePaolo, D., 2018. Fracture evolution in multimineral systems: the role of mineral composition, flow rate, and fracture aperture heterogeneity. ACS Earth Space Chem. 2, 112–124. https://doi.org/10.1021/acsearthspacechem.7b00130.
DePaolo, D.J., Orr, F.M., 2008. Geoscience research for our energy future. Phys. Today 61, 46–51.
Detwiler, R.L., Glass, R.J., Bourcier, W.L., 2003. Experimental observation of fracture dissolution: the role of Peclet number on evolving aperture variability. Geophys. Res. Lett. 30, 1648. https://doi.org/10.1029/2003GL017396.
Dijk, P., Berkowitz, B., 1998. Precipitation and dissolution of reactive solutes in fractures. Water Resour. Res. 34, 457–470.
Elkhoury, J.E., Ameli, P., Detwiler, R.L., 2013. Dissolution and deformation in fractured carbonates caused by flow of CO_2-rich brine under reservoir conditions. Int. J. Greenhouse Gas Control 16S, 203–215.
Garcia-Rios, M., Luquot, L., Soler, J.M., Cama, J., 2017. The role of mineral heterogeneity on the hydrogeochemical response of two fractured reservoir rocks in contact with dissolved CO_2. Appl. Geochem. 84, 202–217. https://doi.org/10.1016/j.apgeochem.2017.06.008.
Golfier, F., Zarcone, C., Bazin, B., Lenormand, R., Lasseux, D., Quintard, M., 2002. On the ability of a Darcy-scale model to capture wormhole formation during the dissolution of a porous medium. J. Fluid Mech. 457, 213–254.
Gouze, P., Noiriel, C., Bruderer, C., Loggia, D., Leprovost, R., 2003. X-ray tomography characterisation of fracture surfaces during dissolution. Geophys. Res. Lett. 30, 1267. https://doi.org/10.1029/2002/GL016755.
Griffiths, L., Heap, M.J., Wang, F., Daval, D., Gilg, H.A., Baud, P., Schmittbuhl, J., Genter, A., 2016. Geothermal implications for fracture-filling hydrothermal precipitation. Geothermics 64, 235–245.
Gupta, N., Balakotaiah, V., 2001. Heat and mass transfer coefficients in catalytic monoliths. Chem. Eng. Sci. 56, 4771–4786.
Hoefner, M.L., Fogler, H.S., 1998. Pore evolution and channel formation during flow and reaction in porous media. AICHE J. 34, 45–53.
Hung, K.M., Sepehrnoori, K., 1989. A mechanistic model of wormhole growth in carbonate matrix acidizing and acid fracturing. J. Pet. Technol. 41, 59–66.
Lasaga, A.C., 1981. Transition state theory. In: Lasaga, A.C., Kirkpatrick, R.J. (Eds.), Kinetics of Geochemical Process. Mineralogical Society of America.
Li, L., Steefel, C.I., Yang, L., 2008. Scale dependence of mineral dissolution rates within single pores and fractures. Geochim. Cosmochim. Acta 72, 360–377.
Luquot, L., Gouze, P., 2009. Experimental determination of porosity and permeability changes induced by injection of CO_2 into carbonate rocks. Chem. Geol. 265, 148–159.
Molins, S., Trebotich, D., Steefel, C.I., Shen, C., 2012. An investigtion of the effect of pore scale flow on average geochemical reaction rates using direct numerical simulation. Water Resour. Res. 48, W03527.
Morse, J.W., Arvidson, R.S., 2002. The dissolution kinetics of major sedimentary carbonate minerals. Earth Sci. Rev. 58, 51–84.
Mourzenko, V.V., Békri, S., Thovert, J.F., Adler, P.M., 1996. Deposition in fractures. Chem. Eng. Commun. 148-150, 431–464.
Noiriel, C., 2015. Resolving time-dependent evolution of pore scale structure, permeability and reactivity using X-ray microtomography. In: Steefel, C.I., Emmanuel, E., Anovitz, L. (Eds.), Pore Scale Geochemical Processes. Reviews in Mineralogy & Geochemistry. vol. 80 Mineralogical Society of America.
Noiriel, C., Daval, D., 2017. Pore-scale geochemical reactivity associated with CO_2 storage: new frontiers at the fluid-solid interface. Acc. Chem. Res. 50, 759–768.
Noiriel, C., Gouze, P., Madé, B., 2007a. Time-resolved 3D characterisation of flow and dissolution patterns in a single rough-walled fracture. In: Krasny, J., Sharp, J. (Eds.), IAH Selected Papers Series 9 on Groundwater in Fractured Rocks. Taylor & Francis.
Noiriel, C., Madé, B., Gouze, P., 2007b. Impact of coating development on the hydraulic and transport properties in argillaceous limestone fracture. Water Resour. Res. 43, W09046. https://doi.org/10.1029/2006WR005379.
Noiriel, C., Gouze, P., Made, B., 2013. 3D analysis of geometry and flow changes in a limestone fracture during dissolution. J. Hydrol. 486, 211–223.
Ortoleva, P., Merino, E., Moore, C., Chadam, J., 1987a. Geochemical self-organization I. Reaction - transport feedbacks and modeling approach. Am. J. Sci. 287, 979–1007.
Ortoleva, P.J., Chadam, J., Merino, E., Sen, A., 1987b. Geochemical self-organization II. The reactive infiltration instability. Am. J. Sci. 287, 1008–1040.
Osselin, F., Kondratiuk, P., Budek, A., Cybulski, O., Garstecki, P., Szymczak, P., 2016. Microfluidic observation of the onset of reactive-infiltration instability in an analog fracture C8 - 2016GL069261. Geophys. Res. Lett. 43, 6907–6915.
Plummer, L.N., Wigley, T.M.L., Parkhurst, D.L., 1978. The kinetics of calcite dissolution in CO_2-water systems at 5° to 60 °C and 0.0 to 1.0 atm CO_2. Am. J. Sci. 278, 179–216.
Pyrak-Nolte, L.J., DePaolo, D.J., Pietraß, T., 2015. Controlling Subsurface Fractures and Fluid Flow: A Basic Research Agenda. USDOE Office of Science (SC) United States.
Renshaw, C.E., 1995. On the relationship between mechanical and hydraulic apertures in rough-walled fractures. J. Geophys. Res. Solid Earth 100, 24629–24636.
Starchenko, V., Marra, C.J., Ladd, A.J.C., 2016. Three-dimensional simulations of fracture dissolution. J. Geophys. Res. Solid Earth 121, 6421–6444.
Steefel, C.I., Lasaga, A.C., 1990. Evolution of dissolution patterns: permeability change due to coupled flow and reaction. In: Melchior, D., Bassett, R.L. (Eds.), Chemical Modeling of Aqueous Systems II. American Chemical Society, Washington DC.
Steefel, C.I., Appelo, C.A.J., Arora, B., Jacques, D., Kalbacher, T., Kolditz, O., Lagneau, V., Lichtner, P.C., Mayer, K.U., Meeussen, J.C.L., Molins, S., Moulton, D., Shao, H., Simunek, J., Spycher, N., Yabusaki, S.B., Yeh, G.T., 2015. Reactive transport codes for subsurface environmental simulation. Comput. Geosci. 19, 445–478.
Szymczak, P., Ladd, A.C.J., 2004. Microscopic simulations of fracture dissolution. Geophys. Res. Lett. 31, L23606. https://doi.org/10.1029/2004GL021297.
Szymczak, P., Ladd, A.J.C., 2009. Wormhole formation in dissolving fractures. J. Geophys. Res. Solid Earth 114, B06203. https://doi.org/10.1029/2008jb006122.
Szymczak, P., Ladd, A., 2012. Reactive-infiltration instabilities in rocks. Fracture dissolution. J. Fluid Mech. 702, 239–264.
Upadhyay, V.K., Szymczak, P., Ladd, A.J.C.C.J.B., 2015. Initial conditions or emergence: what determines dissolution patterns in rough fractures? J. Geophys. Res. Solid Earth 120, 6102–6121.
Zhang, Y., Yang, S., Zhang, S., Mou, J., 2014. Wormhole propagation behavior and its effect on acid leakoff under in situ conditions in acid fracturing. Transp. Porous Media 101, 99–114.
Zimmerman, R.W., Yeo, I., 2000. Fluid flow in rock fractures: from the Navier-Stokes equations to the cubic law. In: Faybishenko, B., Witherspoon, P.A., Benson, S.M. (Eds.), Dynamics of Fluids in Fractured Rocks. Geophysical Monograph 122.